Stochastic inverse modeling of transient laboratory-scale three-dimensional two-phase core flooding scenarios

Authors: A. Dell'Oca[1], A. Manzoni[2*], M. Siena[2*], N. G. Bona[3], L. Moghadasi[3], M. Miarelli[3], D. Renna[3], A. Guadagnini[2]

[1]Institute of Environmental Assessment and Water Research, IDAEA-CSIC, Carrer de Jordi Girona, 18-26, 08304, Barcelona, Spain

[2]Department of Civil and Environmental Engineering, Politecnico di Milano, Piazza Leonardo da Vinci 32, 20133 Milan, Italy

[3]Eni Exploration & Production, Petroleum Engineering Laboratories, 20097 Milan, Italy

*Corresponding author, e-mail: martina.siena@polimi.it, postal address: Department of Civil and Environmental Engineering, Politecnico di Milano, Piazza Leonardo da Vinci 32, 20133 Milan, Italy

*Corresponding author, e-mail: andrea2.manzoni@polimi.it, postal address: Department of Civil and Environmental Engineering, Politecnico di Milano, Piazza Leonardo da Vinci 32, 20133 Milan, Italy

Keywords: Porous media, Transient multiphase flow, Core flooding experiments, Stochastic inverse modeling, Global Sensitivity Analysis.

Highlights:

- Stochastic model calibration is used for three-dimensional transient two-phase flow
- X-ray scanning allows detection of 3D in-situ fluid saturations
- Interpretation of unique data from oil and brine displacement experiments is given
- Coupling of sensitivity analysis with optimization reduces computational costs
- Roles of uncertain model parameters in two-phase systems are quantified

ABSTRACT

We develop a comprehensive and efficient workflow for a stochastic assessment of key parameters governing two-phase flow conditions associated with core-scale experiments. We rely on original and detailed datasets collected on a Berea sandstone sample. These capture the temporal evolution of pressure drop across the core and three-dimensional maps of phase saturations (determined via X-ray CT) in oil- and brine-displacement flooding scenarios characterized by diverse brine/oil viscosity contrasts. Such experiments are used as a test-bed for the proposed stochastic model calibration strategy. The latter is structured across three main steps: (*i*) a preliminary calibration, aimed at identifying a behavioral region of the model parameter space; (*ii*) a Global Sensitivity Analysis (GSA), geared towards identification of the relative importance of model parameters on observed model outputs and assessment of non-influential parameters to reduce dimensionality of the parameter space; and (*iii*) a stochastic inverse modeling procedure. The latter is based on a differential-evolution genetic algorithm to efficiently explore the reduced parameter space stemming from the GSA. It enables one to obtain a probabilistic description of the relevant model parameters through their frequency distributions conditional on the detailed type of information collected. Coupling GSA with a stochastic parameter estimation approach based on a genetic algorithm of the type we consider enables streamlining the procedure and effectively cope with the considerable computational efforts linked to the two-phase scenario considered. Results show a remarkable agreement with experimental data and imbue us with confidence on the potential of the approach to embed the type of rich datasets considered towards model parameter estimation fully including uncertainty.

1. Introduction

Characterization of two-phase flow processes in porous media is key in environmental and industrial scenarios. In this broad context, multiphase flow processes are critically important in driving, e.g., sustainable and enhanced use of underground energy resources (e.g., [1]) .

Real-time three-dimensional (3D) imaging techniques of transient multiphase flow laboratory experiments are becoming increasingly appealing due to their non-invasive nature. A variety of imaging techniques are nowadays applied to study fluid displacement in porous media. These include X-ray Computer Tomography (CT) (e.g., [2–7]) and micro-CT ([8–11]), neutron radiography [12], and magnetic resonance imaging (e.g., [13–17]). A variety of applications of these imaging techniques tackle observation and modeling of multi-phase flow dynamics at the pore-scale (e.g., [9–11]). Here, we focus on continuum-scale patterns of two-phase (oil and brine) flow settings of the kind related to core-flooding experiments.

Saturation data based on 3D core imaging have been recently used to characterize CO_2-brine interaction [5] and waterflood dynamics in oil-displacement experiments [6]. Recently, Fannir et al. (2020) [17] rely on three-dimensional (3D) imaging to assess oil saturation in core scale two-phase oil displacement and quantify some relevant aspects of the setting through a set of dimensionless quantities. Wang et al. (2020) [18] employ 3D images of a CO_2/water core flooding scenario to evaluate the effect of errors caused by simplified modeling of heterogeneous systems. In this context, even as 3D models might be associated with a higher level of operational complexity and computational requirements than their streamlined 1D counterparts, relying on such modeling approaches can provide major insights on the structure of two-phase flow fields that can exhibit complex patterns of displacement fronts due to flow instabilities and/or heterogeneities in the hydraulic properties of the host porous medium (e.g., [2,19,20]).

In this framework, a rigorous and robust approach to quantification of the way uncertainties associated with the key parameters driving the system dynamics are constrained through rich datasets of the kind described above is still lacking. Here, we tackle this objective by merging parallel streams of research. These include Global Sensitivity Analysis (GSA) and stochastic inverse modeling.

Considering GSA (e.g., [21]) enables one to diagnose the behavior of a selected interpretive model as well as the relative contribution of uncertain model parameters to model output uncertainty ([22–27]). Furthermore, it has the additional advantage of being conducive to the identification of non-influential (or only minimally influential) model parameters. This enables streamlining the computational efforts linked to stochastic inverse modeling ([28–33]) upon setting some parameter(s) (which are deemed as uninfluential) at prescribed value(s) without significantly affecting modeling results. Our study is patterned after the approach proposed by Morris (1991) [34]. The latter is a versatile and convenient approach in the presence of highly demanding (in terms of computational effort) model simulations. These types of analyses have been applied to selected basin-scale depositional settings across geologic time scales (e.g., [33] and references therein). Similarly, sensitivity and uncertainty analyses have been recently applied to aid the appraisal of key elements driving the documented complexities associated with multiphase flow through porous media ([35–38]). The solution of an inverse problem is challenging due to a variety of factors, including e.g., issues related to non-uniqueness (see, e.g., [39], and, [37,38]with reference to two-phase flow scenarios). Here, we consider a stochastic inverse modeling framework. As opposed to a deterministic approach, the latter yields probability distributions of uncertain model parameters (i.e., [40,41]). In this sense, one obtains a collection of possible solutions of the inverse problem, each constrained through (i.e., conditional on) the available information content. This approach enables one to provide predictions under uncertainty. The latter is quantified in terms of the above mentioned (posterior) distribution of model parameters, i.e., the probability distribution of parameters conditional to available experimental observations (see e.g., [42,43] for recent applications stochastic inverse modeling approaches).

The study is structured as follows. Section 2 includes a detailed description of the available experimental investigations and the ensuing dataset. It also introduces the methodological workflow, together with key theoretical elements underpinning the selected Global Sensitivity Analysis and stochastic inverse modeling approach. Implementation of the workflow and the ensuing results are discussed in Section 3. Concluding remarks are offered in Section 4.

2. Materials and Methods

The current study relies on a unique set of core-scale data associated with two-phase laboratory-scale flooding experiments (see Sec 2.1 for further details). Available data encompass: (*i*) the temporal history of core-scale pressure drop, i.e., $\Delta\hat{P}_t$ (experimentally observed quantities are hereafter denoted with a hat symbol); and (*ii*) detailed three-dimensional spatial distributions of phase saturations monitored at various times, i.e., $\hat{S}_{\alpha,i,t}$ (subscripts α, i, and t referring to fluid phase, a generic location across the core sample, and time, respectively). While measurements of $\Delta\hat{P}_t$ are commonly available in flooding experiments to support characterization of rock sample attributes, observations about $\hat{S}_{\alpha,i,t}$ are seldom available (e.g., [44]). These provide a unique source of information on transient two-phase flow dynamics. Such a rich base of information is here used to design a workflow conducive to improved characterization of the hydraulic properties of rock samples within a stochastic inverse modeling context.

From a conceptual point of view, we interpret the transient two-phase flow dynamics at the continuum scale through a set of commonly used balance equations and constitutive relationships (see Sec. 2.2) which are then solved numerically. The selected mathematical formulation includes *N* model parameters θ_j (j = 1, ..., N) collected in vector $\boldsymbol{\theta}$. These embed salient features of processes relevant to the two-phase flood scenario (e.g., relative permeabilities and parameters of the associated formulations) and are here treated as random quantities. Thus, we aim at characterizing the probability density function (*pdf*) of $\boldsymbol{\theta}$ by leveraging on the unique information content associated with the available experimental dataset. To accomplish this objective, we design an operational workflow merging (*a*) Stochastic Model Calibration (SMC) (see Sec. 2.3) and (*b*) Global Sensitivity Analysis (GSA) (see Sec. 2.4), as detailed in the following. Relying on this strategy enables us to cope with the computational burden related to SMC. The latter might indeed become markedly high in the presence of a large set of parameters because of the computational cost associated with forward numerical simulations of the three-dimensional transient two-phase flow scenario we tackle.

Fig. 1 provides a sketch of the workflow adopted in our study. We start by defining the support space of the random model parameters, i.e., $\boldsymbol{\Gamma} = \Gamma_{\theta_1} \times ... \times \Gamma_{\theta_N}$. At this stage, each parameter θ_j is treated as an independent random variable uniformly distributed within the support Γ_{θ_j}. The latter is assessed on the basis of available literature information and/or expert opinion. We then perform a preliminary model calibration upon estimating model parameters across $\boldsymbol{\Gamma}$. This is aimed at providing: (*i*) a set of model parameters compatible (in terms of the value of the objective function defined in Sec. 2.3) with the available observations, and (*ii*) a reference value for the objective function that corresponds to a satisfactory degree of consistency with the experimental data. The results of this step enable us to define a *behavioral* parameter space, i.e., $\boldsymbol{\Gamma^B}$. We then perform a GSA focused on ΔP_t and $S_{\alpha,i,t}$ (i.e., the model-based counterparts of $\Delta\hat{P}_t$ and $\hat{S}_{\alpha,i,t}$) across such space. In this second stage, we revise the parameter support ranges. This ensures that the collection of the numerical simulations upon which the GSA is grounded are consistent with the experimental observations, in the sense that the salient qualitative features of $\Delta\hat{P}_t$ and $\hat{S}_{\alpha,i,t}$ are reproduced with a satisfactory quantitative agreement between numerical results and their experimental counterparts.

Thus, we tie the GSA results to the available experimental evidence and rely on the ensuing analysis to (eventually) identify model parameters that can be deemed as non-influential for ΔP_t and $S_{\alpha,i,t}$. Doing so yields a secondary parameter support space (hereafter denoted as $\boldsymbol{\Gamma}'$) that includes only model parameters that are identified as influential. Stochastic model calibration is then performed within $\boldsymbol{\Gamma}'$. This allows identifying sample frequency distributions of influential model parameters conditional on the available data (non-influential parameters being set at the values obtained from the preliminary model calibration). Note that, as further detailed in Sec. 2.3, we leverage on the reference value of the objective function obtained in the preliminary model calibration to define a stopping criterion during the stochastic model calibration stage.

2.1. Experimental set up

Fig. 2a depicts a schematic representation of the experimental setup. Key elements include a core holder, an X-ray apparatus for in-situ detection of fluid saturation, and differential pressure transducers. The experiments are performed on a cylindrical core of Berea sandstone, whose key properties are listed in Table 1. Prior to starting the tests, the core sample is cleaned, washed, and scanned via X-ray CT (NSI X-5000 tomograph; North Star Imaging) at dry and fully brine-saturated conditions (i.e., S_b = 1). All of the acquired scans are post-processed (we use a Lanczos filter to this end; see , e.g., [45]) to obtain a voxel resolution of 0.24 mm^3. The latter is then lowered (through the application of a triangular re-sampling filter) to obtain a spatial resolution of 0.997 × 0.993 × 0.996 mm^3. This enables estimating absolute permeability, K, and assessing the distribution of porosity, $\hat{\phi}_i$, (depicted in Fig. 2b), for each voxel i according to which the system is discretized as:

$$\hat{\phi}_i = c \cdot (\tau_{b,i} - \tau_{a,i}) \tag{1}$$

where $\tau_{a,i}$ and $\tau_{b,i}$ are the i-th voxel linear attenuation coefficient at air- or brine-saturated conditions respectively. Fig. 2b depicts the spatial distribution of the porosity at the sub-sample scale. An inspection of the latter highlights the presence of 3D heterogeneous features across the sample, i.e., tilted planes characterized by higher values of porosity. A pore volume (PV) of 38.2 ml is estimated upon relying on saturation data collected during brine injection, considering the linear relationship between brine saturation and total injected volume (before brine breakthrough):

$$\langle S_b(t)\rangle - \langle S_b(t_0)\rangle = Q_b \frac{(t-t_0)}{PV} \tag{2}$$

where $\langle\ \rangle$ denotes arithmetic average over all sample voxels, $\langle S_b(t)\rangle$ and $\langle S_b(t_0)\rangle$ represent the average brine saturations at time t and t_0 (i.e., the initial average brine saturation in the sample), respectively; and Q_b is the brine volumetric flow rate. The ratio between the PV and the total core volume provides an estimate of the average core-scale porosity of the sample (here $\langle\hat{\phi}\rangle \approx 0.17$). Note that the value of c in Eq. (1) is assessed as $c = \langle\tau_{b,i} - \tau_{a,i}\rangle/\langle\hat{\phi}\rangle$.

Two unsteady-state displacement tests have been performed on the core. The first experiment corresponds to an oil-displacement setting, in which a low-viscosity (LV) oil (soltrol 130) is displaced by injecting brine in the sample. Note that, to mimic a typical reservoir scenario, the oil initially in place in this experiment is the result of an injection in a preliminary brine-saturated pore space. The second experiment corresponds to a brine-displacement scenario. Here, a high viscosity (HV) oil (OBI 10) is injected into the initially fully brine-saturated sample. Note that the core was washed before each experiment. Density and viscosity of the fluids employed in the experiments are listed in Table 2. Brine composition is characterized by NaCl (84.36 g/L), $CaCl_2$ (23.12 g/L), KCl (32.14 g/L), and NaI (54.09 g/L). The latter is used to enhance X-ray contrast between water and oil phase, to improve measurement accuracy. A constant temperature of 30 °C is maintained in both experiments. Fluid injection takes place from the bottom of the sample. Pressure difference between core inlet and outlet is continuously monitored. Ambient pressure is maintained at the outlet section. The temporally-varying spatial distribution of oil saturation is monitored periodically via X-Ray CT scans. As an example, Fig. 2 collects three-dimensional spatial distributions of oil saturation corresponding to three observation times during the oil- (Fig. 2c) and brine-displacement (Fig. 2d) experiments. Visual inspection of the 3D maps of oil saturation reveals the presence of sub-sample heterogeneities. It can be seen that the displacement front appears to be quite dispersed during the oil-displacement (low viscosity contrast). Otherwise, the front transition is sharper during the brine-displacement (high stabilizing viscosity contrast) while being clearly non-uniform along the transverse cross-section as a consequence of the spatially heterogeneous nature of the hydraulic properties of the sample. The X-Ray beam employed to infer oil saturation is generated by applying an electric potential of 140 kV. A scan time of 15 min is used to collect high-quality images and is employed at the equilibrium or for slow changes in saturation distribution. Otherwise, in the transient regime we take scans every 1 min and 13 s, to enhance characterization of the rapidly-evolving fluid dynamics. As a consequence, we expect the acquisitions in the transient time frame to be more affected by experimental errors than their steady state counterparts. This issue has been considered in the definition of the objective function to be minimized in the model calibration process (see Sec. 2.3).

2.2 Two-phase flow model

Mass conservation for each (incompressible) fluid phase α reads

$$\phi \frac{\partial}{\partial t}(S_\alpha) + \nabla \cdot (\boldsymbol{q}_\alpha) = 0 \tag{3}$$

where, ϕ [-] is the (spatially variable, see Sec. 2.1) porosity; S_α [-] is saturation of fluid phase α; $\boldsymbol{q}_\alpha$ [LT^{-1}] is the extended Darcy flux vector for fluid phase α, which can be expressed as

$$\boldsymbol{q}_\alpha = -\frac{\boldsymbol{k} k_{r\alpha}}{\mu_\alpha}(\nabla P_\alpha - \rho_\alpha \boldsymbol{g}) \tag{4}$$

where $\boldsymbol{k}$ [L^2] is the absolute permeability tensor; $k_{r\alpha}$ [-] is relative permeability for fluid phase α; P_α [$ML^{-1}T^{-2}$], μ_α [$ML^{-1}T^{-1}$], and ρ_α [ML^{-3}] are pressure, dynamic viscosity, and density of phase α, respectively; and $\boldsymbol{g}$ [LT^{-2}] is gravity. Note that we consider a two-phase system composed by brine ($\alpha = b$) and oil ($\alpha = o$). Saturation of the two phases must satisfy

$$S_b + S_o = 1 \tag{5}$$

Solutions of Eqs. (3)-(5) require an additional constraint. The latter concerns the capillary pressure, $P_c(S_b)$ [$ML^{-1}T^{-2}$], (i.e., the pressure difference across the interface between the two-phases in the system), which can be expressed as a function of brine saturation. Preliminary tests of the calibration framework aimed at evaluating the potential ability of various P_c (S_b) formulations to grasp the main patterns associated with the experimental observations revealed that a numerical solution consistent with the available datasets could be obtained only by considering negligible capillary effects (details not shown).

Absolute permeability is treated as isotropic and spatially heterogeneous, i.e., $\boldsymbol{k}(\boldsymbol{x}) = \boldsymbol{I}k(\boldsymbol{x})$, where $\boldsymbol{I}$ is the identity matrix. We leverage on the knowledge about the spatial distribution of porosity across the core to (at least partially) capture the heterogeneous distribution of k which can then be considered in the inverse modeling context. To this end, we employ the following widely used relationship [43]:

$$log_{10}(k) = m\phi + w \tag{6}$$

Note that k appearing in Eq. (6) is expressed in m^2. We include m [-] in our probabilistic analysis workflow. Otherwise, we set w = -16 (which is equivalent to imposing a permeability of 0.1 mD for porosity values that tend to 0) based on a series of previous applications of Eq. (6) to interpret an extensive set of core-scale two-phase flow experiments performed on several Berea samples at the internal experimental facilities in ENI, Italy (not shown). These imbue us with prior knowledge to guide the modeling choice about w.

With reference to relative permeability, we recall that a variety of empirical formulations are available to render the dependence of relative permeability on the degree of fluid saturation (e.g., [7,44,46–50]). Here, we rely on the Corey formulation [46] due to its simplicity and parsimony (in terms of the number of parameters that are to be estimated), i.e.,

$$k_{rb} = k_{rb}^{*}(S_b^{*})^{N_b} \tag{7}$$

$$k_{ro} = k_{ro}^{*}(1 - S_b^{*})^{N_0} \tag{8}$$

Here, k_{rb}^{*} [-] and k_{ro}^{*} [-] are the end-point relative permeabilities for brine and oil, respectively; N_b [-] and N_0[-] are exponents; and S_b^{*} is the normalized brine saturation, i.e.,

$$S_b^{*} = \frac{S_b - S_b^{irr}}{1 - S_b^{irr} - S_{or}} \tag{9}$$

where S_b^{irr} [-] and S_{or} [-] are the irreducible brine and residual oil saturations, respectively. Note that we treat S_b^{irr} as a spatially heterogeneous quantity, by viewing it as a fraction (i.e., through a proportionality factor, F_r) of (*i*) the initial brine saturation in the oil-displacement scenario; or (*ii*) the steady-state brine saturation, for the brine-displacement experiment. The heterogeneous distribution of S_{or} is assessed according to the formulation of Spiteri (2008) [51], i.e.,

$$S_{or} = \xi(\gamma)S_{oin} - \beta(\gamma)S_{oin}^2 \tag{10}$$

where the coefficients $\xi(\gamma)$ [-] and $\beta(\gamma)$ [-] are functions of the contact angle, i.e., γ[-] ([52]; see Fig. 10), and S_{oin} is the initial oil saturation.

In summary, the two-phase flow model detailed in Eqs. (3)-(10) embeds a total of N = 7 parameters, i.e., $\boldsymbol{\theta} = (m, k_{rb}^*, k_{ro}^*, N_b, N_0, F_r, \gamma)$. These are then subject to estimation through stochastic model calibration (see Sec. 2.3).

Various open-source numerical codes are available to cope with transient two-phase flow settings (e.g. [20,53]). Similar to Manasipov et al. (2020) [54], we solve the transient two-phase flow scenario associated with Eqs. (3)-(10) upon relying on the well known and widely tested open-source Matlab Reservoir Simulation Toolbox (MRST, see [55]) environment in light of its straightforward adaptability to our context. We employ the finite volume discretization method with a two-point flux-approximation scheme, as embedded in MRST. Consistent with the previously noted spatial heterogeneity of the sub-sample hydraulic properties that, in turns, impacts the dynamics of the displacing front (see Sec. 2.1 and Fig. 2), we employ a three-dimensional (structured Cartesian) grid. The latter comprises $N_v = 720$ elements of size 6.88 mm^3. We test the robustness of the employed discretization upon considering several synthetic scenarios (characterized by various combinations of the model parameters) designed considering the same geometry of the Berea sample and the same initial conditions in terms of phase saturations employed in the experiments. We obtain satisfactory stochastic calibrations at an affordable computational burden for all of the scenarios analyzed, thus imbuing us with confidence about the selected discretization (see [56]). Note that we transfer the (spatially variable) experimental values of porosity and phase saturations obtained at the original spatial resolution (see Sec. 2.1) to the one associated with the adopted computational grid to ensure consistency between observations and numerical results. For simplicity, we do so upon relying on a straightforward arithmetic and weighted (by the porosity) averaging approach for the porosity and the phase saturations, respectively.

2.3. Stochastic Model Calibration

Model calibration is grounded on the minimization of the following objective function

$$J(\boldsymbol{\theta}) = W_S \frac{\sum_t^{N_{ts}} \sum_i^{N_v} \left(\hat{S}_{o,i,t} - S_{o,i,t}(\boldsymbol{\theta})\right)^2}{N_{ts} N_v} + W_P \frac{\sum_t^{N_{tp}} \left(\frac{\Delta\hat{P}_t - \Delta P_t(\boldsymbol{\theta})}{\Delta\hat{P}_{max}}\right)^2}{N_{tp}} + W_{S_{ss}} \frac{\sum_i^{N_v} \left(\hat{S}_{o,i,ss} - S_{o,i,ss}(\boldsymbol{\theta})\right)^2}{N_v} \quad (11)$$

$\Delta P_t(\boldsymbol{\theta})$ and $S_{o,i,t}(\boldsymbol{\theta})$ corresponding to model outputs at the N_{ts} and N_{tp} experimental observation times for the phase saturations and core-scale pressure drop, respectively; $S_{o,i,ss}(\boldsymbol{\theta})$ is the oil saturation under steady-state condition; $\Delta\hat{P}_{max}$ is the maximum value of the measured pressure drop; and W_s,W_P, and $W_{S_{ss}}$ are the weights of the terms appearing in the objective function. These typically depend on the experimental error affecting $\hat{S}_{o,i,t}$, $\Delta\hat{P}_t$, and $\hat{S}_{o,i,ss}$, respectively. We recall here that a common working assumption relies on considering a Gaussian probability distribution to characterize measurement errors (e.g., [39]). At the same time, we also note that the exact values of the standard deviation of the latter are rarely known. Thus, various combinations of the values of the weights in Eq. (11) are typically tested to determine their optimal values (see e.g., [38]). Distinct triplets of the weights - i.e., $\left(W_s = W_{S_{ss}} = W_P = 1\right)$, $\left(W_s = W_{S_{ss}} = 1;\, W_P = 10\right)$ and $\left(W_s = 1; W_{S_{ss}} = W_P = 10\right)$ - have been analyzed in a preliminary study. The analysis revealed that (a) the magnitude of the errors associated with transient and steady-state saturations (i.e., $S_{o,i,t}$ and $S_{o,i,ss}$) does not vary significantly across the set of triplets ($W_s, W_P, W_{S_{ss}}$); (b) the residual associated with ΔP_t decreases as $W_{S_{ss}}$ and W_P increase. The latter finding is consistent with the higher degree of reliability associated with the experimental values of $\Delta\hat{P}_t$ and $\hat{S}_{o,i,ss}$ relative to those of $\hat{S}_{o,i,t}$.

In this context, minimization of Eq. (11) with respect to $\boldsymbol{\theta}$ is performed through a Differential Evolution (DE) algorithm (e.g., [57]). The latter is a direct-search method in which one starts upon introducing a population, $\boldsymbol{S}$, of candidate solutions composed by N_S members (where each member, $\boldsymbol{s}_i$, is a vector of dimension N_m). In the present context, a member of the population represents a possible model parameter combination, $\boldsymbol{\theta}$. Hence, $N_m = N = 7$. We implement the algorithm according to [57] and set $N_S = 10 \times N = 70$. The initial population of candidate solutions, i.e., $\boldsymbol{S}^{\mathbf{0}} = [\boldsymbol{s}_1^0, \ldots, \boldsymbol{s}_{Ns}^0]$, is defined by randomly selecting the j-th element of the i-th member, $s_{i,j}^0$ (for $j = 1, \ldots, N$ and $i = 1, \ldots, N_S$), from the support Γ_{θ_j} of the model parameter θ_j. This enables the DE algorithm to be initialized through a uniform coverage of the parameter space. At a subsequent k-th step, the members of the population are updated to obtain $\boldsymbol{S}^k = [\boldsymbol{s}_1^k, \ldots, \boldsymbol{s}_{Ns}^k]$ by selecting the i-th member $\boldsymbol{s}_i^k$ between (i) a trial member $\tilde{\boldsymbol{s}}_i^k$ and (ii) the i-th population member at the previous step, $\boldsymbol{s}_i^{k-1}$, according to

$$\boldsymbol{s}_i^k = \begin{cases} \tilde{\boldsymbol{s}}_i^k, & J(\tilde{\boldsymbol{s}}_i^k) < J(\boldsymbol{s}_i^{k-1}) \\ \boldsymbol{s}_i^{k-1}, & J(\tilde{\boldsymbol{s}}_i^k) \geq J(\boldsymbol{s}_i^{k-1}) \end{cases} \tag{12}$$

We recall that the trial member $\tilde{\boldsymbol{s}}_i^k$ is determined as a mutation of $\boldsymbol{s}_i^{k-1}$. The algorithm randomly determines which of the N elements of $\boldsymbol{s}_i^{k-1}$ undergoes a mutation according to the following: (i) a random sample $\boldsymbol{r} \sim U(0,1)^N$ is drawn; (ii) mutations take place only for the elements of $\boldsymbol{s}_i^{k-1}$ for which the corresponding elements of $\boldsymbol{r}$ are smaller than a given crossover value, CR, the mutating elements of $\boldsymbol{s}_i^{k-1}$ being collected in the indexing vector $\bar{\jmath}$; (iii) the values of the mutating elements of $\boldsymbol{s}_i^{k-1}$ are determined according to

$$\tilde{\boldsymbol{s}}(\bar{\jmath})_i^k = \boldsymbol{s}(\bar{\jmath})_i^{k-1} + F \cdot (\boldsymbol{s}(\bar{\jmath})_a^{k-1} - \boldsymbol{s}(\bar{\jmath})_b^{k-1}) \tag{13}$$

where F is a DE algorithm parameter called *differential weight* and $\boldsymbol{s}(\bar{\jmath})_a^{k-1}$ and $\boldsymbol{s}(\bar{\jmath})_b^{k-1}$ (with a, $b \neq i$) correspond to two random members of the population. Considering the results obtained on the synthetic scenarios (discussed above), we set $CR = 0.3$ and $F = 0.4$.

The DE algorithm is employed in the preliminary model calibration step as well as in the final stochastic model calibration (see Fig. 1). In our implementation of the preliminary calibration, we terminate the algorithm when the value of the objective function in Eq. (11) does not vary over 50 consecutive iterations. We do so for simplicity and considering that only a single parameter combination is required in this phase. Otherwise, when tackling the final stochastic model calibration phase, we end the progress of the DE algorithm when the objective function attains a value which is 5% larger than the reference value obtained from the preliminary calibration. We recall that our ultimate purpose is to obtain a distribution of (influential) model parameter values conditional on available information through the imposed convergence criterion. As such the strategy we consider enables one to avoid many model iterations within a region of the parameter space where the objective function does not change significantly, while still maintaining a satisfactory consistency between model results and experimental data. We remark that in this context our results can be interpreted in terms of a frequency distribution of a collection of model parameter estimates. These can then be employed to propagate residual (i.e., after calibration on available data) parameter uncertainty onto target model outputs.

2.4 Global Sensitivity Analysis

The computational burden required to estimate empirical frequency distributions of uncertain model parameters can be alleviated by reducing the dimensionality of the parameter space. This can be accomplished through a rigorous sensitivity analysis. The latter is aimed at diagnosing the model behavior in the presence of uncertain parameters and enables us to discriminate between (*i*) non-influential and (*ii*) influential sets of parameters (with respect to the simulated state variables of interest, i.e., $\Delta P_t, S_{o,i,t}$).

We note that during the identification of non-influential parameters one cannot disregard the experimental evidence about the two-phase flow dynamics taking place in the particular core-sample under investigation. Thus, one needs to guarantee that the set of model simulations upon which the sensitivity analysis is grounded are *behavioral* (see e.g., [58–60]), in the sense that the set of ensuing model outputs must be consistent with their experimental counterparts. We ensure this aspect by demarcating a *behavioral* parameters space (also referred as *active subspace*), $\boldsymbol{\Gamma}^{\boldsymbol{B}} = \Gamma_{\theta_1}^{B} \times \ldots \times \Gamma_{\theta_N}^{B}$, where $\Gamma_{\theta_i}^{B}$ is the *behavioral* support (or range of values) of the *i*-th parameter. This *behavioral* parameter space is only employed to perform the sensitivity analysis. We design it through a simple trial-and-error procedure. We select candidate upper and lower bounds of $\boldsymbol{\Gamma}^{\boldsymbol{B}}$ by acknowledging (*i*) the results of the preliminary model calibration and (*ii*) the corresponding model outputs. We then ensure that the whole set of model simulations upon which the sensitivity analysis is grounded are indeed *behavioral*. Due to the limited number of model simulations required by the selected sensitivity analysis (see below), we ensure the latter requirement by the simple inspection of the juxtaposition of the set of model results and their experimental counterparts. In the event that some simulations lead to unacceptable results (e.g., very distinct trends associated with the time evolution of the core scale pressure drop), we proceed to manually adjusting the extent of $\boldsymbol{\Gamma}^{\boldsymbol{B}}$ to ensure that all of the sampled parameter combinations lead to *behavioral* responses. Moreover, the ranges of the *behavioral* space are also controlled after the stochastic calibration step, i.e., we check that for each *i*-th parameter the probability associated with values outside the support range $\Gamma_{\theta_i}^{B}$ tend to be lowest (ideally null). While more complex and automated approaches are available in the literature for the definition of $\boldsymbol{\Gamma}^{\boldsymbol{B}}$ (e.g., [61] and references therein), we note that the associated computational burden is typically higher and can possibly reduced through the introduction of a surrogate model. Thus, here we prefer to rely on a simple trial-and-error approach with an affordable computational cost.

Considering a model output of interest, $y(\boldsymbol{\theta})$, it is possible to evaluate the so-called elementary effect associated with the *j*-th uncertain model parameter θ_j as

$$EE_{\theta_j} = \frac{y(\theta_1, \dots, \theta_j + \Delta\theta_j, \dots, \theta_N) - y(\theta_1, \dots, \theta_j, \dots, \theta_N)}{\Delta\theta_j} \tag{14}$$

The value of EE_{θ_j} is a *local* (in the parameter space) measure of the sensitivity of y with respect to θ_j, that is quantified in terms of the variation in the value of the former due to a variation of the latter. A *global* measure of sensitivity is obtained upon evaluating the elementary effect (EE_{θ_j}) for a variety of model parameter combinations. To this end we rely on the radial-sampling strategy detailed in [62]. Key summary statistics of the ensuing distribution of EE_{θ_j} are then evaluated, such as [34] and [62]:

$$\mu^*_{\theta_j} = \frac{1}{M}\sum_{k=1}^{M} |EE^k_{\theta_j}| \tag{15}$$

$$\sigma_{\theta_j} = \sqrt{\frac{1}{M}\sum_{k=1}^{M} \left(EE^k_{\theta_j} - \mu^*_{\theta_j}\right)^2} \tag{16}$$

where M is the number of values of EE_{θ_j} associated with θ_j. The quantities $\mu^*_{\theta_j}$ (15) and σ_{θ_j} (16) are estimates of the mean and standard deviation of the distribution of EE_{θ_j}. Note that the absolute value is introduced for the evaluation of $\mu^*_{\theta_j}$ to avoid compensation between positive and negative valued EE_{θ_j}. Non-influential parameters are then characterized by low values of $\mu^*_{\theta_j}$ (i.e., variations of θ_j do not correspond to significant variations in y). A high value of σ_{θ_j} indicates that θ_j influences y in a non-linear fashion or through interactions with other model parameters. Thus, inspection of the Morris' indices (15)-(16) enables us to identify non-influential model parameters at an affordable computational cost (see also [63] and references therein). We follow the sampling strategy proposed by [64] for each experimental scenario. We then find that 80 parameters combinations within $\boldsymbol{\Gamma}^{\boldsymbol{B}}$ are sufficient to yield robust evaluations of the Morris' indices. We then set the identified non-influential parameters to the value associated with their counterparts obtained during the preliminary calibration. We perform the final stochastic model calibration upon considering the parameter space of reduced dimensionality, i.e., $\boldsymbol{\Gamma}'$. The extent of the support of the influential parameters within $\boldsymbol{\Gamma}'$ coincides with its counterpart in $\boldsymbol{\Gamma}$, while the non-influential parameters are set at the values obtained from the preliminary model calibration (we recall here that the numerosity of the population in the DE algorithm scales with N, i.e., the dimensionality of the space within which solutions are searched, see Sec. 2.3).

3. Results

In this Section we detail our results for the (*i*) oil-displacement and (*ii*) brine-displacement experiments.

3.1. Oil-displacement scenario

As detailed in Section 2.1, available observations comprise three-dimensional distributions of: (*i*) porosity across the core sample; and oil saturation (*ii*) at the beginning of the experiment, and during the (*iii*) transient (for a total of six observation windows) and (*iv*) the stationary regime. We complement this information with temporal histories of the core-scale pressure drop. During the experiment brine is injected at a constant flow rate of 15 ml/h.

As a first step in the workflow (see Fig. 1), we perform a preliminary model calibration upon relying on the parameter space $\boldsymbol{\Gamma}$ (see Table 3) and leveraging on the DE algorithm (see Sec. 2.3). Considering the stopping criterion stated in Sec. 2.3 yields a total of 183 model iterations (attaining a final value of the objective function J = 0.0096). The resulting combination of parameter values is listed in Table 3. The corresponding model results are depicted in Fig. 3. The latter includes (*a*) core-scale pressure drop versus time (blue and red curves corresponding to experimental data, $\Delta\hat{P}_t$, and numerical results ΔP_t, respectively); (*b*) scatter plots of simulated ($S_{o,i,t}$) versus measured ($\hat{S}_{o,i,t}$) oil saturations at each voxel of the simulation grid and for the available acquisition times. Inspection of Figs. 3a-3b denotes an overall satisfactory agreement between experimental and numerical results that imbues us with confidence on the appropriateness of this preliminary model calibration step. At the same time, we note that our model tends to underestimate the steady state oil distribution. This might be due to some restriction in the former to rend the full dynamics of the oil-displacement experiment.

We then evaluate the Morris' indexes (see Sec. 2.4) by considering the behavioral parameter space $\boldsymbol{\Gamma}^{\mathbf{B}}$ (see Table 3). Fig. 4 depicts the values of $\mu^*_{\theta_j}$ and σ_{θ_j} associated with temporal dynamics of (*a*) section-averaged oil saturations (which are here considered for ease of representation, as opposed to their three-dimensional counterparts) and (*b*) pressure drop. Inspection of Fig. 4 reveals that (*i*) $[k^*_{ro}, m, \gamma]$ and (*ii*) $[k^*_{ro}, \gamma]$ are characterized by small values of both $\mu^*_{\theta_j}$and σ_{θ_j}. Hence, we regard these sets of parameters as non-influential with respect to the spatial distribution of saturation (Fig. 4a) and pressure drop (Fig. 4b), respectively. We interpret these results by recalling that: (*i*) parameter m has a marked influence on the distribution of the absolute permeability and thus on the corresponding pressure drop required to sustain water flow through the sample; (*ii*) variations of γ across Γ_{γ}^{B} do not lead to significant variations of ξ and β (see also [39]) and therefore do not impact markedly on the investigated system state variables; (*iii*) according with Corey's formulation (Eq. (8)) k_{ro} depends linearly on k_{ro}^{*} (consistent with the small values of $\sigma_{k_{ro}^{*}}$ depicted in Fig. 4a). Moreover, the low oil saturations recorded (see Figs. 2c and 3b) during the oil-displacement experiment is associated with a low relative permeability of this phase, i.e., $k_{ro} \approx 0$. Thus, variations in k_{ro}^{*} within $\Gamma_{k_{ro}^{*}}^{B}$ have a limited effect on k_{ro} and, consequently, on the simulated state variables (as indicated by the small values of $\mu_{k_{ro}^{*}}^{*}$ in Fig. 4a). Eqs. (8)-(9) highlight that the exponent N_o controls the (nonlinear) variation of k_{ro} with the normalized oil saturation, $S_o^* = 1 - S_b^*$. This observation in consistent with the high values of σ_{N_o} for $S_{o,i,t}$ in Fig. 4a.

This set of results leads us to consider k_{ro}^{*} and γ as non-influential. In the stochastic model calibration stage, we set $k_{ro}^{*} = 0.01$ and γ = 146.76 (as obtained from the preliminary model calibration) and focus on $(m, k_{rb}^{*}, N_b, N_o, F_r)$ to minimize the objective function in Eq. (11) within the support $\boldsymbol{\Gamma'}$ (see Table 3). Following the DE algorithm convergence criterion (Sec. 2.3), Fig. 5 depicts the empirical frequency distributions for $(m, k_{rb}^{*}, N_b, N_o, F_r)$ obtained on the basis of 100 inverse modeling solutions (vertical red lines demarcate the bounds of $\boldsymbol{\Gamma^B}$). Inspection of Fig. 5 suggests that: (*i*) most of the instances of the frequency distribution of each parameter are confined within the bounds of $\boldsymbol{\Gamma^B}$, supporting the selected ranges for the GSA; (*ii*) the frequency distributions for *m* and k_{rb}^{*} display well defined peaks, in agreement with the high sensitivity of ΔP_t to these parameters (see Fig. 4b) and with the weight associated with pressure data in the objective function in Eq. (11); and (*iii*) the wide range of values spanned by the frequency distribution of N_o seems to be consistent with the low impact of this parameter on ΔP_t (see Fig. 4b) as well as with the high value of σ_{N_o} (Fig. 4a). The latter element suggests the presence of a non-linear contribution to the impact of N_o on $S_{o,i,t}$, or the effect of interactions between N_o and other model parameters. As such, it is possible that the combination of these two factors could lead to a higher uncertainty for N_o than for the other parameters. We further note that F_r is characterized by a similar behavior to that observed for N_o. Finally, the presence of a sharp peak in the empirical frequency distribution of N_b does not seem to correlate with a high sensitivity of ΔP_t and/or $S_{o,i,t}$ (see Fig. 4) with respect to this parameter (note that ΔP_t is still sensitive to N_b, sensitivity being a necessary while otherwise not a sufficient condition for parameter identifiability, see e.g., [65], [66]). For completeness, in Appendix A we investigate the cross correlation for the estimated parameters that are relevant for the oil-displacement experiment.

3.2. Brine-displacement experiment

The brine-displacement experiment is designed upon setting a lower injection rate (i.e., 2 ml/h) of the invading phase than in the oil-displacement scenario. This enables us to collect (*i*) 14 snapshots of three-dimensional spatial distributions of oil saturation during the transient regime and (*ii*) one image under stationary conditions, in addition to continuously recorded core-scale pressure drop.

Following our workflow, we obtain a first set of model parameters compatible with the experimental observations through a preliminary model calibration relying on the parameter space $\boldsymbol{\Gamma}$ (see Table 4). Achievement of convergence of the DE algorithm (according to the criterion outlined in Sec. 2.3) require a total of 118 iterations (attaining J = 0.020). Note that the high density and viscosity of the oil injected in the brine-displacement experiment leads to a reduced degree of control on the experimental value of the flow rate, some mild fluctuations being observed during the course of the experiment. This might hinder the quality of the match between ΔP_t and $\Delta \hat{P}_t$ (see Fig. 6a), as also suggested by the increased value of J documented here as compared against its counterpart for the oil-displacement scenario.

The resulting parameter combination is listed in Table 4. The corresponding inverse modeling results are collected in Figs. 6a, 6b. The former depicts core-scale pressure drop versus time (blue and red curves corresponding to experimental data and numerical results, respectively). The latter shows a scatter plot of simulated versus observed oil saturations at each voxel and for all acquisition times (i.e., $S_{o,i,t}$ versus $\hat{S}_{o,i,t}$). Inspection of Fig. 6 suggests an overall satisfactory agreement between experimental and numerical results stemming from the preliminary model calibration. Moreover, we note that the strong viscosity contrast leads to a sharp interface between the invading oil and the displaced brine phase. The latter behavior is visible from the experimental results collected in Fig. 2d. It is also clearly documented in Fig. 6b, where it is possible to recognize a set of voxels characterized by (*i*) high or (*ii*) low oil saturation (i.e., upstream and downstream region of the advancing front), jointly with (*iii*) a decreased amount of voxels characterized by intermediate values of saturation (i.e., at locations corresponding to the front region) as compared to the oil-displacement experiment. It is observed that the numerical results tend to overestimate the degree of oil saturation, especially during the initial period of the experiment (i.e., until approximately 7080 s) when high values of oil saturation are observed. This observation suggests that during the early stages the numerical model tends to render the advancement of the oil front at a rate that is faster than its experimentally observed counterpart. Nevertheless, there is a markedly high consistency between model results and experimental oil phase saturation values at steady state.

We then evaluate the Morris' indices by considering the behavioral parameter space $\boldsymbol{\Gamma^B}$ (see Table 4). Fig. 7 depicts the values of $\mu^*_{\theta_j}$ and σ_{θ_j} for (*a*) (section-averaged) oil saturation (as a function of time and depth along the core) and (*b*) pressure drop across the core. Inspection of Figs. 7a-7b reveals that N_o and γ exhibit a very limited influence on both state variables. In contrast with what observed for the oil-displacement experiment, we obtain low values also for σ_{N_o}. We interpret this result by considering that, due to the higher viscosity contrast, the advancing front is considerably sharper in the brine-displacement than in the oil-displacement scenario (see Figs. 2c and 2d). As a consequence, there is a lower portion of voxels that is characterized by intermediate values of $S_{o,i,t}$. Thus, variations in N_o (i.e., in the relative permeability curve far from the endpoints) are not associated with marked variations of the system dynamics. Another difference with respect to the oil-displacement experiment is that $S_{o,i,t}$ increases progressively in time and assumes values in the whole range [0, 1]. For these reasons (*i*) the quantity S_{or} is not relevant in the description of this experiment, consistent with the low impact of γ (see Eq. (10)) and (*ii*) the oil phase is characterized by a non-negligible relative permeability ($k_{ro} \gg 0$). This makes k^*_{ro} an influential parameter, in particular for the pressure drop (see Fig. 7b).

We then complete the stochastic model calibration stage by focusing on the reduced parameter space $(N_b, k^*_{rb}, k^*_{ro}, m, F_r)$. We minimize the objective function Eq. (11) within the support $\boldsymbol{\Gamma}'$ (see Table 4) while setting N_o and γ to the values obtained in the preliminary model calibration step. Fig. 8 depicts the empirical frequency distributions (grounded on 100 inverse modeling solutions) for $(N_b, k^*_{rb}, k^*_{ro}, m, F_r)$ (vertical red lines correspond to the bounds of $\boldsymbol{\Gamma}^{\boldsymbol{B}}$). Most of the frequency distributions obtained are contained within the limits of $\boldsymbol{\Gamma}^{\boldsymbol{B}}$, some exceptions being noted for k^*_{ro} and m. This observation suggests that, for these parameters, the actual behavioral ranges could be wider than those considered in the GSA. Furthermore, the frequency distributions for the influential parameters tend to be more broadly distributed than their counterparts obtained in the oil-displacement experiment. This result can be attributed to the generally lower degree of sensitivity of ΔP_t and $S_{o,i,t}$ with respect to the influential parameters, as quantified by the values of $\mu^*_{\theta_j}$ and σ_{θ_j} (Fig. 7) when compared to those resulting for the oil-displacement experiment (Fig. 4). This, in turn, prevents the identification of a clear peak in the resulting frequency distributions of the parameters. Considering the constraint associated with Eqs. (8) and (9), the parameter sets obtained lead to a sustained increase in oil relative permeability with oil saturation, i.e., relative oil permeability is significantly higher than the water relative permeability for intermediate and high oil saturations. For completeness, in Appendix A we investigate the cross correlation for the estimated parameters that are relevant for the brine-displacement experiment.

4. Conclusions

We propose a novel stochastic inverse modeling framework to assist interpretation laboratory-scale two-phase fluid displacement experiments. Our methodology is conducive to frequency distributions of model parameters and combines the Differential Evolution optimization algorithm and the use of Morris' indices for global sensitivity analysis (GSA). Including GSA in the workflow enables us to mitigate the challenges related to large computational costs typically associated with the application of population-based optimization algorithms in stochastic inverse settings.

The methodology is applied to interpret uniquely rich datasets. These include detailed temporal series of (*i*) three-dimensional spatial distributions of phase saturations and (*ii*) core-scale pressure drops. To cover a wide variety of scenarios, two sets of experiments are analyzed. These encompass an oil-displacement and a brine-displacement scenario, characterized by different density and viscosity contrasts between brine and oil. Our work leads to the following major conclusions.

1. The results of our analyses clearly show that assisting stochastic inverse modeling through Global Sensitivity Analysis can considerably contribute to (*a*) clarification and quantification of the role of uncertain model parameters in driving the two-phase system dynamics and (*b*) reduction of the dimensionality of the uncertain model parameter space. The latter is a critical element to be considered in the context of a computationally intensive forward modeling scenario of the kind we consider.
2. Amongst the uncertain model parameters embedded in the formulation considered, only 5 have been recognized as key sources of uncertainties significantly affecting the prediction of model outputs (i.e., temporal histories of detailed three-dimensional distribution of fluid saturations and pressure drop across the sample). These relevant parameters include, for both the experiments, the coefficient m in the porosity/permeability relationship (Eq. (6)); k_{rb}^{*} and N_b, controlling brine relative permeability curve (Eq. (7)); and F_r, associated with the irreducible brine saturation (Eq. (9)). Moreover, N_o appeared to be relevant only in the oil-displacement scenario, while k_{ro}^{*} affected appreciably the model outputs only in the brine-displacement experiment.
3. The amount of information employed in the stochastic model calibration is very detailed and consistent with modern experimental capabilities. Our study fully takes advantage of these experimental evidences and provides a comprehensive analysis of the dynamics of two-phase flow in fractured/porous media. In all cases investigated, the stochastic approach is documented to be effective to identify frequency distributions of model parameters rendering a satisfactory agreement between experimental and numerical results (in a probabilistic sense). It forms a robust basis to

effectively assist (*a*) interpretation of data associated with coreflooding practices, (*b*) further design of laboratory coreflooding experiments.

From a practical perspective, the proposed workflow is structured across various steps (spanning from a preliminary model calibration to a stochastic calibration) to readily assist the efficient assessment of probability distributions of model parameters upon leveraging on the information content of the available experimental observations. We recall here that the workflow is fully compatible with the use of alternative specific techniques to complement those we selected in our application. For example, one can embed (*i*) other models for relative permeability curves (e.g., the LET model of [67]); (*ii*) different GSA approaches (e.g., the moment-based sensitivity indices of [27]) for parameter screening; or (*iii*) other stochastic calibration strategies (e.g., Monte Carlo Markov Chain as in [35,36]). The layout selected for the current applications is inspired by our expertise and knowledge and aims at attaining a balance among a variety of factors including, e.g., the representativeness of the numerical modeling approach, its accuracy and the associated computational burden. The latter might be reduced through the introduction of a surrogate model (e.g., [27,35,36,68]). Otherwise, it is remarked that the efficient assessment of a surrogate model for time-dependent quantities, such as three-dimensional fluid phase distributions, is a non-trivial task. Thus, we opted to rely on the numerical model detailed in Sec. 2.2 across the various steps of the proposed workflow for the current application while deferring to future studies the detailed analysis of the effects of introducing a surrogate model.

CRediT author statement:

A. Dell'Oca: Conceptualization, Methodology, Software, Validation, Formal analysis, Writing - Original Draft, Writing - Review & Editing; **A. Manzoni**: Conceptualization, Methodology, Software, Validation, Formal analysis, Writing - Original Draft, Writing - Review & Editing; **M. Siena**: Conceptualization, Methodology, Software, Writing - Original Draft, Writing - Review & Editing; **N. G. Bona:** Investigation, Data Curation, Writing - Review & Editing, Supervision; L. **Moghadasi:** Investigation, Data Curation, Writing - Review & Editing; **M. Miarelli:** Investigation, Data Curation, Writing - Review & Editing; **D. Renna:** Investigation, Data Curation, Writing - Review & Editing; **A.**

Guadagnini: Conceptualization, Methodology, Validation, Formal analysis, Writing - Original Draft, Writing - Review & Editing, Supervision.

Acknowledgments

Funding was provided by Eni. A.D. acknowledges the funding by the European Commission through the Marie Sklodowska-Curie Individual Fellowship, research project 'MixUQ' Grant Agreement No. 895152. The software developed in this study (4D-CoreINV) is protected by copyright.

Appendix A. Estimated parameters cross correlations

Figure A1 depicts the scatter plots between the sets of calibrated parameters for (*a*) the oil- and (*b*) the brine-displacement scenario, respectively. Inspection of Fig. A1a does not reveal any clear degree of correlation between the pairwise sets of estimated parameters, with the sole exception of N_o and F_r that appear to display a mild positive correlation. The emergence of such pattern is imprinted/driven by the information content provided by the available data. It suggests that oil displacement in case of an increased brine saturation (corresponding to an increase of N_o) tends to be harder when the fraction of irreducible brine increases (i.e., F_r increases). Otherwise, inspection of Fig. A1b suggests a negative correlation between N_b and F_r. This reflects a tendency towards a facilitated displacement of brine (i.e., a decrease of N_b) as the irreducible water content increases (i.e., F_r increases). Stochastic model calibration on the available data also suggests that the coefficient *m* is (*i*) negatively correlated with k_{rb}^*, k_{ro}^* and (*ii*) positively correlated with N_b. These results denote a tendency to balance between those parameters that control the overall resistance to flow of the fluid phases through the sample, i.e., the absolute values of the permeabilities (an increase in *m* leads to a reduced flow resistance) and the values attained by k_{rb}^* (higher values lead to less flow resistance) and N_b (lower values correspond to less flow resistance) for the brine and the values of k_{ro}^* (higher values lead to less flow resistance) for the oil phase. The same type of conceptual picture could be associated with the positive correlation that is noted between k_{rb}^* and k_{ro}^*. Overall, these sets of results highlight that parameters associated with an equifinality (in particular with respect to the core-scale pressure drop) are harder to be identified for our two scenarios, especially for the brine-displacement scenario (note that parameters displaying correlation with some others tend to be characterized by broad frequency distributions; see Fig. A1).

References

[1] M. Taheriotaghsara, Enhanced oil recovery methods targeting danish north sea chalk reservoirs PhD Thesis, Denmark Technical University, 2020.

[2] S. Berg, S. Oedai, H. Ott, Displacement and mass transfer between saturated and unsaturated CO2–brine systems in sandstone, International Journal of Greenhouse Gas Control. 12 (2013) 478–492. https://doi.org/10.1016/j.ijggc.2011.04.005.

[3] S.C.M. Krevor, R. Pini, L. Zuo, S.M. Benson, Relative permeability and trapping of CO_2 and water in sandstone rocks at reservoir conditions, Water Resour Res. 48 (2012). https://doi.org/10.1029/2011WR010859.

[4] T. Kurotori, R. Pini, A general capillary equilibrium model to describe drainage experiments in heterogeneous laboratory rock cores, Adv Water Resour. 152 (2021) 103938. https://doi.org/10.1016/j.advwatres.2021.103938.

[5] K.-Y. Kim, J. Oh, W.S. Han, K.G. Park, Y.J. Shinn, E. Park, Two-phase flow visualization under reservoir conditions for highly heterogeneous conglomerate rock: A core-scale study for geologic carbon storage, Sci Rep. 8 (2018) 4869. https://doi.org/10.1038/s41598-018-23224-6.

[6] M. Mascle, E. Rosenberg, B. Roboele, E. Kowalewski, S. Youssef, Investigation of waterflood front digitations during immiscible displacements in porous media, Oil & Gas Science and Technology – Revue d'IFP Energies Nouvelles. 76 (2021) 71. https://doi.org/10.2516/ogst/2021053.

[7] L. Moghadasi, A. Guadagnini, F. Inzoli, M. Bartosek, D. Renna, Characterization of two- and three-phase relative permeability of water-wet porous media through X-Ray saturation measurements, J Pet Sci Eng. 145 (2016) 453–463. https://doi.org/10.1016/j.petrol.2016.05.031.

[8] M.J. Blunt, B. Bijeljic, H. Dong, O. Gharbi, S. Iglauer, P. Mostaghimi, A. Paluszny, C. Pentland, Pore-scale imaging and modelling, Adv Water Resour. 51 (2013) 197–216. https://doi.org/10.1016/j.advwatres.2012.03.003.

[9] L. Leu, S. Berg, F. Enzmann, R.T. Armstrong, M. Kersten, Fast X-ray Micro-Tomography of Multiphase Flow in Berea Sandstone: A Sensitivity Study on Image Processing, Transp Porous Media. 105 (2014) 451–469. https://doi.org/10.1007/s11242-014-0378-4.

[10] M. Andrew, H. Menke, M.J. Blunt, B. Bijeljic, The Imaging of Dynamic Multiphase Fluid Flow Using Synchrotron-Based X-ray Microtomography at Reservoir Conditions, Transp Porous Media. 110 (2015) 1–24. https://doi.org/10.1007/s11242-015-0553-2.

[11] S. Hasan, V. Niasar, N.K. Karadimitriou, J.R.A. Godinho, N.T. Vo, S. An, A. Rabbani, H. Steeb, Direct characterization of solute transport in unsaturated porous media using fast X-ray synchrotron microtomography, Proceedings of the National Academy of Sciences. 117 (2020) 23443–23449. https://doi.org/10.1073/pnas.2011716117.

[12] Y. Zhao, S. Xue, S. Han, L. He, Z. Chen, Characterization of unsaturated diffusivity of tight sandstones using neutron radiography, Int J Heat Mass Transf. 124 (2018) 693–705. https://doi.org/10.1016/j.ijheatmasstransfer.2018.03.090.

[13] S. Chen, K.-H. Kim, F. Qin, A.T. Watson, Quantitative NMR imaging of multiphase flow in porous media, Magn Reson Imaging. 10 (1992) 815–826. https://doi.org/10.1016/0730-725X(92)90417-X.

[14] Y. Zhao, Y. Song, Y. Liu, H. Liang, B. Dou, Visualization and Measurement of CO_2 Flooding in Porous Media Using MRI, Ind Eng Chem Res. 50 (2011) 4707–4715. https://doi.org/10.1021/ie1013019.

[15] Y. Song, L. Jiang, Y. Liu, M. Yang, Y. Zhao, N. Zhu, B. Dou, A. Abudula, An experimental study on CO2/water displacement in porous media using high-resolution Magnetic Resonance Imaging, International Journal of Greenhouse Gas Control. 10 (2012) 501–509. https://doi.org/10.1016/j.ijggc.2012.07.017.

[16] M. Li, L. Romero-Zerón, F. Marica, B.J. Balcom, Polymer Flooding Enhanced Oil Recovery Evaluated with Magnetic Resonance Imaging and Relaxation Time Measurements, Energy & Fuels. 31 (2017) 4904–4914. https://doi.org/10.1021/acs.energyfuels.7b00030.

[17] J. Fannir, I. Panfilova, S. Leclerc, D. Stemmelen, Studying of parameters of two-phase displacement in porous media with MRI technique, Mechanics & Industry. 21 (2020) 524. https://doi.org/10.1051/meca/2020058.

[18] D. Wang, Z. Zheng, Q. Ma, P. Hu, X. Huang, Y. Song, Effects of the errors between core heterogeneity and the simplified models on numerical modeling of CO2/water core flooding, Int J Heat Mass Transf. 149 (2020) 119223. https://doi.org/10.1016/j.ijheatmasstransfer.2019.119223.

[19] M.S. Krause, S. Krevor, J.C. Perrin, R. Pini, S. Benson, A Procedure for Accurate Determination of Sub-Core Scale Permeability Distributions with Error Quantification, in: 7 Th Annual GCEP Research Symposium, 2011.

[20] J.G. Maas, N. Springer, A. Hebing, Defining a sample heterogeneity cut-off value to obtain representative Special Core Analysis (SCAL) measurements, in: International Symposium of the Society of Core Analysts Held in Pau, France, 2019: pp. 26 Aug.-30 Aug.

[21] A. Saltelli, M. Ratto, T. Andres, F. Campolongo, J. Cariboni, D. Gatelli, M. Saisana, S. Tarantola, Global sensitivity analysis: The primer, John Wiley & Sons, Ltd, Chichester, UK, 2008. https://doi.org/10.1002/9780470725184.

[22] M.K. Muleta, J.W. Nicklow, Sensitivity and uncertainty analysis coupled with automatic calibration for a distributed watershed model, J Hydrol (Amst). 306 (2005) 127–145. https://doi.org/10.1016/j.jhydrol.2004.09.005.

[23] F. Pappenberger, K.J. Beven, M. Ratto, P. Matgen, Multi-method global sensitivity analysis of flood inundation models, Adv Water Resour. 31 (2008) 1–14. https://doi.org/10.1016/j.advwatres.2007.04.009.

[24] T. Wagener, K. van Werkhoven, P. Reed, Y. Tang, Multiobjective sensitivity analysis to understand the information content in streamflow observations for distributed watershed modeling, Water Resour Res. 45 (2009). https://doi.org/10.1029/2008WR007347.

[25] M.V. Ruano, J. Ribes, A. Seco, J. Ferrer, An improved sampling strategy based on trajectory design for application of the Morris method to systems with many input factors, Environmental Modelling & Software. 37 (2012) 103–109. https://doi.org/10.1016/j.envsoft.2012.03.008.

[26] E. Hill, M.C. Foglia, S. Christensen, O. Rakovec, Model Validation, in: The Handbook of Groundwater Engineering, CRC Press, Taylor & Francis Group, 6000 Broken Sound Parkway NW, Suite 300, Boca Raton, FL 33487-2742, 2016: pp. 597–620. https://doi.org/10.1201/9781315371801-22.

[27] A. Dell'Oca, M. Riva, A. Guadagnini, Moment-based metrics for global sensitivity analysis of hydrological systems, Hydrol Earth Syst Sci. 21 (2017) 6219–6234. https://doi.org/10.5194/hess-21-6219-2017.

[28] D. Degenring, C. Froemel, G. Dikta, R. Takors, Sensitivity analysis for the reduction of complex metabolism models, J Process Control. 14 (2004) 729–745. https://doi.org/10.1016/j.jprocont.2003.12.008.

[29] A. van Griensven, T. Meixner, S. Grunwald, T. Bishop, M. Diluzio, R. Srinivasan, A global sensitivity analysis tool for the parameters of multi-variable catchment models, J Hydrol (Amst). 324 (2006) 10–23. https://doi.org/10.1016/j.jhydrol.2005.09.008.

[30] J. Nossent, P. Elsen, W. Bauwens, Sobol' sensitivity analysis of a complex environmental model, Environmental Modelling & Software. 26 (2011) 1515–1525. https://doi.org/10.1016/j.envsoft.2011.08.010.

[31] J. Chu, C. Zhang, G. Fu, Y. Li, H. Zhou, Improving multi-objective reservoir operation optimization with sensitivity-informed dimension reduction, Hydrol Earth Syst Sci. 19 (2015) 3557–3570. https://doi.org/10.5194/hess-19-3557-2015.

[32] V. Punzo, M. Montanino, B. Ciuffo, Do We Really Need to Calibrate All the Parameters? Variance-Based Sensitivity Analysis to Simplify Microscopic Traffic Flow Models, IEEE Transactions on Intelligent Transportation Systems. 16 (2015) 184–193. https://doi.org/10.1109/TITS.2014.2331453.

[33] S.E. Patani, G.M. Porta, V. Caronni, P. Ruffo, A. Guadagnini, Stochastic Inverse Modeling and Parametric Uncertainty of Sediment Deposition Processes Across Geologic Time Scales, Math Geosci. 53 (2021) 1101–1124. https://doi.org/10.1007/s11004-020-09911-z.

[34] M.D. Morris, Factorial Sampling Plans for Preliminary Computational Experiments, Technometrics. 33 (1991) 161. https://doi.org/10.2307/1269043.

[35] A.R. Valdez, B.M. Rocha, G. Chapiro, R. Weber dos Santos, Uncertainty quantification and sensitivity analysis for relative permeability models of two-phase flow in porous media, J Pet Sci Eng. 192 (2020) 107297. https://doi.org/10.1016/j.petrol.2020.107297.

[36] A.R. Valdez, B.M. Rocha, J.M. da Fonseca Façanha, A.V.O. de Souza, A. Pérez-Gramatges, G. Chapiro, R.W. dos Santos, Foam-Assisted Water–Gas Flow Parameters:

From Core-Flood Experiment to Uncertainty Quantification and Sensitivity Analysis, Transp Porous Media. 144 (2022) 189–209. https://doi.org/10.1007/s11242-021-01550-0.

[37] S. Berg, E. Unsal, H. Dijk, Non-uniqueness and uncertainty quantification of relative permeability measurements by inverse modelling, Comput Geotech. 132 (2021) 103964. https://doi.org/10.1016/j.compgeo.2020.103964.

[38] S. Berg, E. Unsal, H. Dijk, Sensitivity and Uncertainty Analysis for Parameterization of Multiphase Flow Models, Transp Porous Media. 140 (2021) 27–57. https://doi.org/10.1007/s11242-021-01576-4.

[39] J. Carrera, S.P. Neuman, Estimation of Aquifer Parameters Under Transient and Steady State Conditions: 1. Maximum Likelihood Method Incorporating Prior Information, Water Resour Res. 22 (1986) 199–210. https://doi.org/10.1029/WR022i002p00199.

[40] A. Tarantola, Inverse Problem Theory and Methods for Model Parameter Estimation, Society for Industrial and Applied Mathematics, 2005. https://doi.org/10.1137/1.9780898717921.

[41] H. Zhou, J.J. Gómez-Hernández, L. Li, Inverse methods in hydrogeology: Evolution and recent trends, Adv Water Resour. 63 (2014) 22–37. https://doi.org/10.1016/j.advwatres.2013.10.014.

[42] L. Ceresa, A. Guadagnini, G.M. Porta, M. Riva, Formulation and probabilistic assessment of reversible biodegradation pathway of Diclofenac in groundwater, Water Res. 204 (2021) 117466. https://doi.org/10.1016/j.watres.2021.117466.

[43] A. Timur, An investigation of permeability, porosity, and residual water saturation relationships, in: SPWLA 9th Annu. Logging Symp., 1968.

[44] G.L. Chierici, Novel Relations for Drainage and Imbibition Relative Permeabilities, Society of Petroleum Engineers Journal. 24 (1984) 275–276. https://doi.org/10.2118/10165-PA.

[45] C.E. Duchon, Lanczos filtering in one and two dimensions, Journal of Applied Meteorology. 19 (1979).

[46] A.T. Corey, The interrelation between gas and oil relative permeabilities, Prod. Mon. (1954) 38–41.

[47] M.R.J. Wyllie, A Note on the Interrelationship Between Wetting and Nonwetting Phase Relative Permeability, Journal of Petroleum Technology. 3 (1951) 17–17. https://doi.org/10.2118/951381-G.

[48] M. Honarpour, L.F. Koederitz, A.H. Harvey, Empirical Equations for Estimating Two-Phase Relative Permeability in Consolidated Rock, Journal of Petroleum Technology. 34 (1982) 2905–2908. https://doi.org/10.2118/9966-PA.

[49] P. Xu, S. Qiu, B. Yu, Z. Jiang, Prediction of relative permeability in unsaturated porous media with a fractal approach, Int J Heat Mass Transf. 64 (2013) 829–837. https://doi.org/10.1016/j.ijheatmasstransfer.2013.05.003.

[50] E. Bianchi Janetti, M. Riva, A. Guadagnini, Effects of Pore-Scale Geometry and Wettability on Two-Phase Relative Permeabilities within Elementary Cells, Water (Basel). 9 (2017) 252. https://doi.org/10.3390/w9040252.

[51] E.J. Spiteri, R. Juanes, M.J. Blunt, F.M. Orr, A New Model of Trapping and Relative Permeability Hysteresis for All Wettability Characteristics, SPE Journal. 13 (2008) 277–288. https://doi.org/10.2118/96448-PA.

[52] E.J. Spiteri, R. Juanes, M.J. Blunt, F.M. Orr, A new model of trapping and relative permeability hysteresis for all wettability characteristics, SPE Journal. 13 (2008) 277–288. https://doi.org/10.2118/96448-PA.

[53] J.M.M. Regtien, G.J.A. Por, M.T. van Stiphout, F.F. van der Vlugt, Interactive Reservoir Simulation, in: All Days, SPE, 1995. https://doi.org/10.2118/29146-MS.

[54] R. Manasipov, B. Jenei, Automated Interpretation Tool for Synchronous History Matching of Multiple Scal Experiments with Advance Nurbs Representations of Relevant Functions, in: Day 3 Thu, December 03, 2020, SPE, 2020. https://doi.org/10.2118/200559-MS.

[55] K.-A. Lie, An Introduction to Reservoir Simulation Using MATLAB/GNU Octave, Cambridge University Press, 2019. https://doi.org/10.1017/9781108591416.

[56] A. Manzoni, Three-dimensional inverse modelling of two-phase flows at the core scale, Politecnico di Milano, 2020.

[57] R. Storn, K. Price, A Simple and Efficient Heuristic for Global Optimization over Continuous Spaces, Journal of Global Optimization. 11 (1997) 341–359. https://doi.org/10.1023/A:1008202821328.

[58] M. Teixeira Parente, S. Mattis, S. Gupta, C. Deusner, B. Wohlmuth, Efficient parameter estimation for a methane hydrate model with active subspaces, Comput Geosci. 23 (2019) 355–372. https://doi.org/10.1007/s10596-018-9769-x.

[59] D. Erdal, O.A. Cirpka, Technical Note: Improved sampling of behavioral subsurface flow model parameters using active subspaces, Hydrol Earth Syst Sci. 24 (2020) 4567–4574. https://doi.org/10.5194/hess-24-4567-2020.

[60] D. Erdal, O.A. Cirpka, Global sensitivity analysis and adaptive stochastic sampling of a subsurface-flow model using active subspaces, Hydrol Earth Syst Sci. 23 (2019) 3787–3805. https://doi.org/10.5194/hess-23-3787-2019.

[61] D. Erdal, O.A. Cirpka, Technical Note: Improved sampling of behavioral subsurface flow model parameters using active subspaces, Hydrol Earth Syst Sci. 24 (2020) 4567–4574. https://doi.org/10.5194/hess-24-4567-2020.

[62] F. Campolongo, J. Cariboni, A. Saltelli, An effective screening design for sensitivity analysis of large models, Environmental Modelling & Software. 22 (2007) 1509–1518. https://doi.org/10.1016/j.envsoft.2006.10.004.

[63] G. Porta, D. la Cecilia, A. Guadagnini, F. Maggi, Implications of uncertain bioreactive parameters on a complex reaction network of atrazine biodegradation in soil, Adv Water Resour. 121 (2018) 263–276. https://doi.org/10.1016/j.advwatres.2018.08.002.

[64] F. Campolongo, A. Saltelli, J. Cariboni, From screening to quantitative sensitivity analysis. A unified approach, Comput Phys Commun. 182 (2011) 978–988. https://doi.org/10.1016/j.cpc.2010.12.039.

[65] H. v. Gupta, S. Razavi, Revisiting the Basis of Sensitivity Analysis for Dynamical Earth System Models, Water Resour Res. 54 (2018) 8692–8717. https://doi.org/10.1029/2018WR022668.

[66] R. Brun, P. Reichert, H.R. Künsch, Practical identifiability analysis of large environmental simulation models, Water Resour Res. 37 (2001) 1015–1030. https://doi.org/10.1029/2000WR900350.

[67] F. Lomeland, E. Ebeltoft, W.H. Thomas, A New Versatile Relative Permeability Correlation History matching View project Curve fitting flow functions View project Frode Lomeland OREC AS-Consultants Einar Ebeltoft A NEW VERSATILE RELATIVE PERMEABILITY CORRELATION, 2005. https://www.researchgate.net/publication/242724867.

[68] M. Riva, A. Guadagnini, A. Dell'Oca, Probabilistic assessment of seawater intrusion under multiple sources of uncertainty, Adv Water Resour. 75 (2015) 93–104. https://doi.org/10.1016/j.advwatres.2014.11.002.

Figures

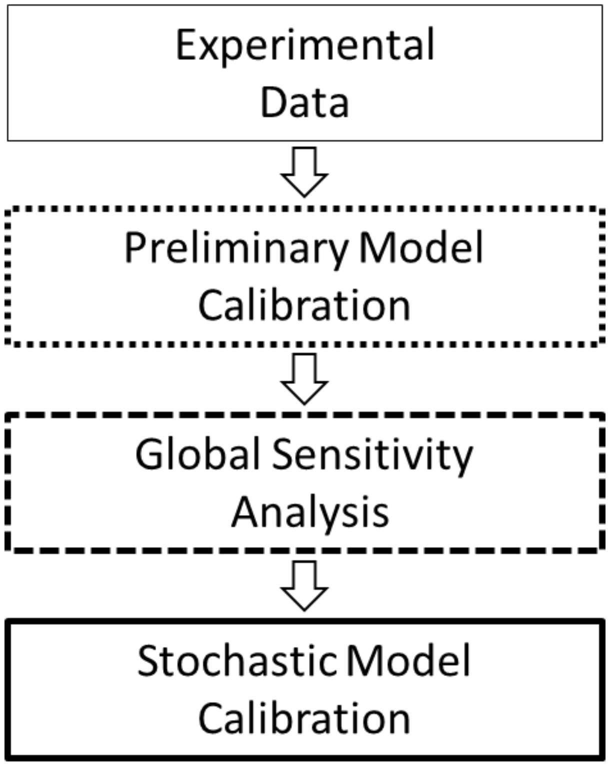

Fig. 1. Sketch of the proposed workflow: (*i*) collection of experimental datasets; (*ii*) preliminary model calibration to assess a plausible combination of parameters (see Sec. 2.3); (*iii*) Global Sensitivity Analysis (see Sec. 2.4) across a behavioral parameter space to identify influential parameters; (*iv*) Stochastic model calibration to assess frequency distributions of influential model parameters (see Sec. 2.4).

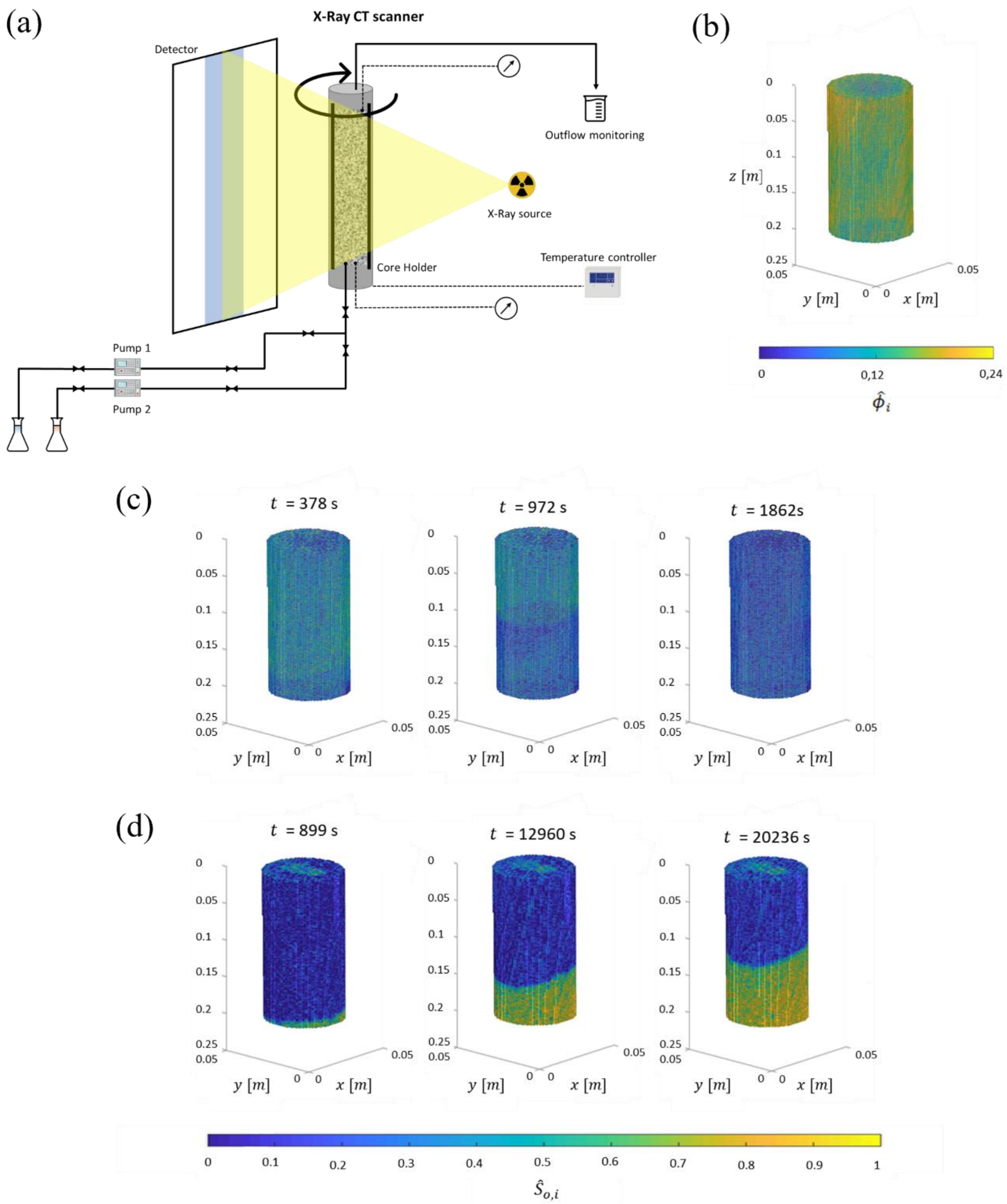

Fig. 2. Sketch of the experimental set-up (*a*); three-dimensional distributions of sample porosity, $\hat{\phi}_i$ (*b*); three-dimensional distributions of oil saturation, $\hat{S}_{o,i,t}$, at various acquisition times for the oil- (*c*) and brine- (*d*) displacement experiments. Spatial resolution associated with experimental data is 0.997 × 0.993 × 0.996 mm^3.

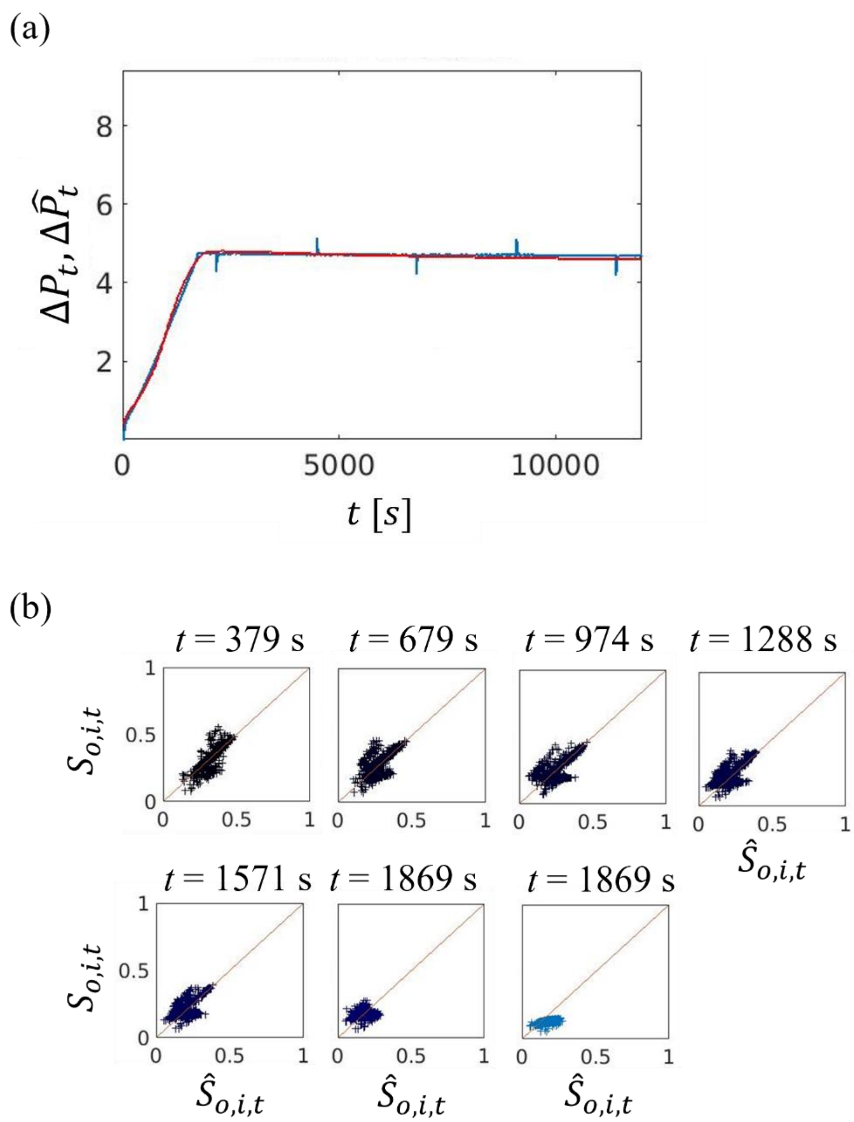

Fig. 3. Application of the proposed workflow to the oil-displacement scenario. Preliminary model calibration results: (*a*) experimental ($\Delta\hat{P}_t$, blue curve) and numerical (ΔP_t, red curve) temporal pattern of core-scale pressure drop; (*b*) scatter plots of experimental oil saturations ($\hat{S}_{o,i,t}$) versus their numerical counterparts ($S_{o,i,t}$, symbols) at available observation times.

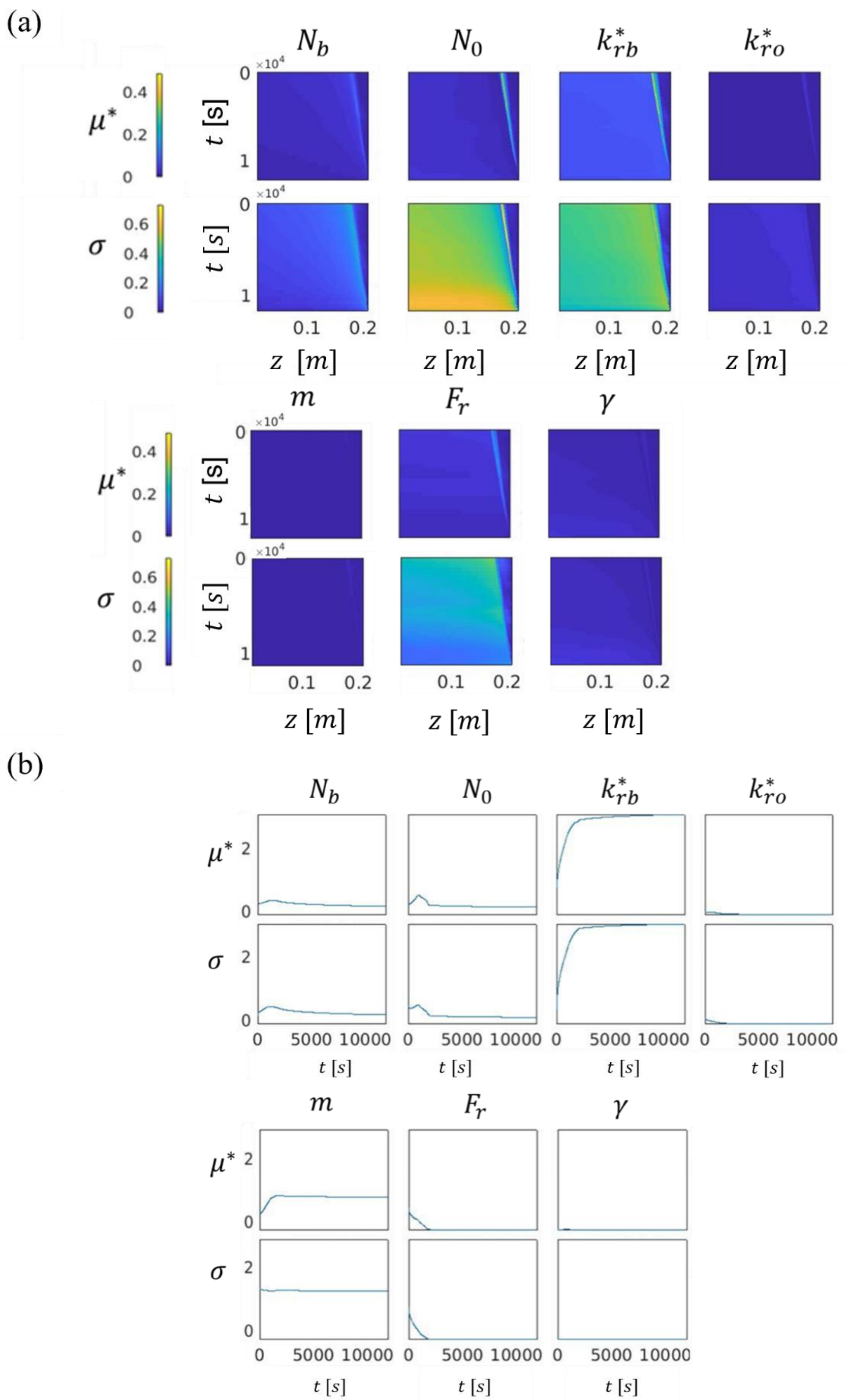

Fig. 4. Application of the proposed workflow for the oil-displacement scenario. Global Sensitivity Analysis results: Morris' sensitivity indices (i.e., $\mu^*_{\theta_j}$ (15) and σ_{θ_j} (16)) for (*a*) (section-averaged) oil saturation and (*b*) core-scale pressure drop.

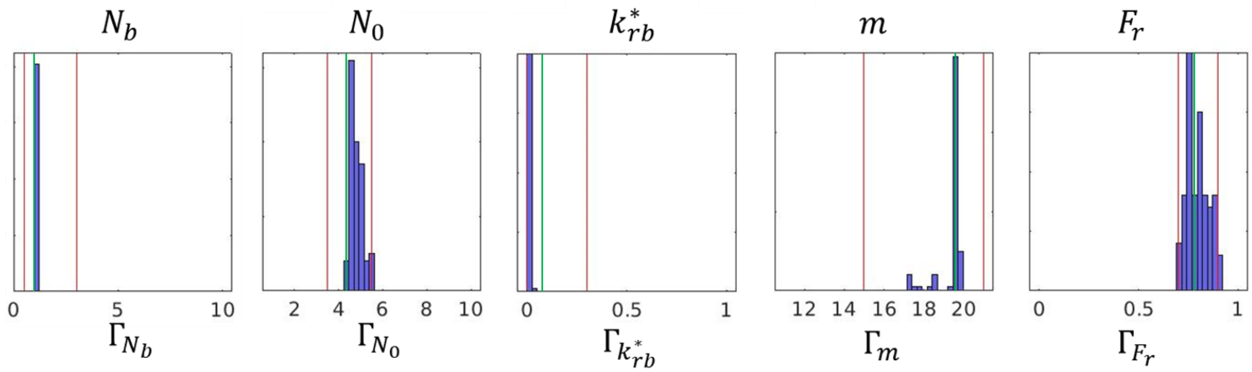

Fig. 5. Application of the proposed workflow for the oil-displacement scenario. Stochastic model calibration results: empirical frequency distributions for the set influential parameters (see Table 3). Red lines indicate the boundaries of the corresponding behavioral range; the green line correspond to the parameter values obtained through the preliminary model calibration stage.

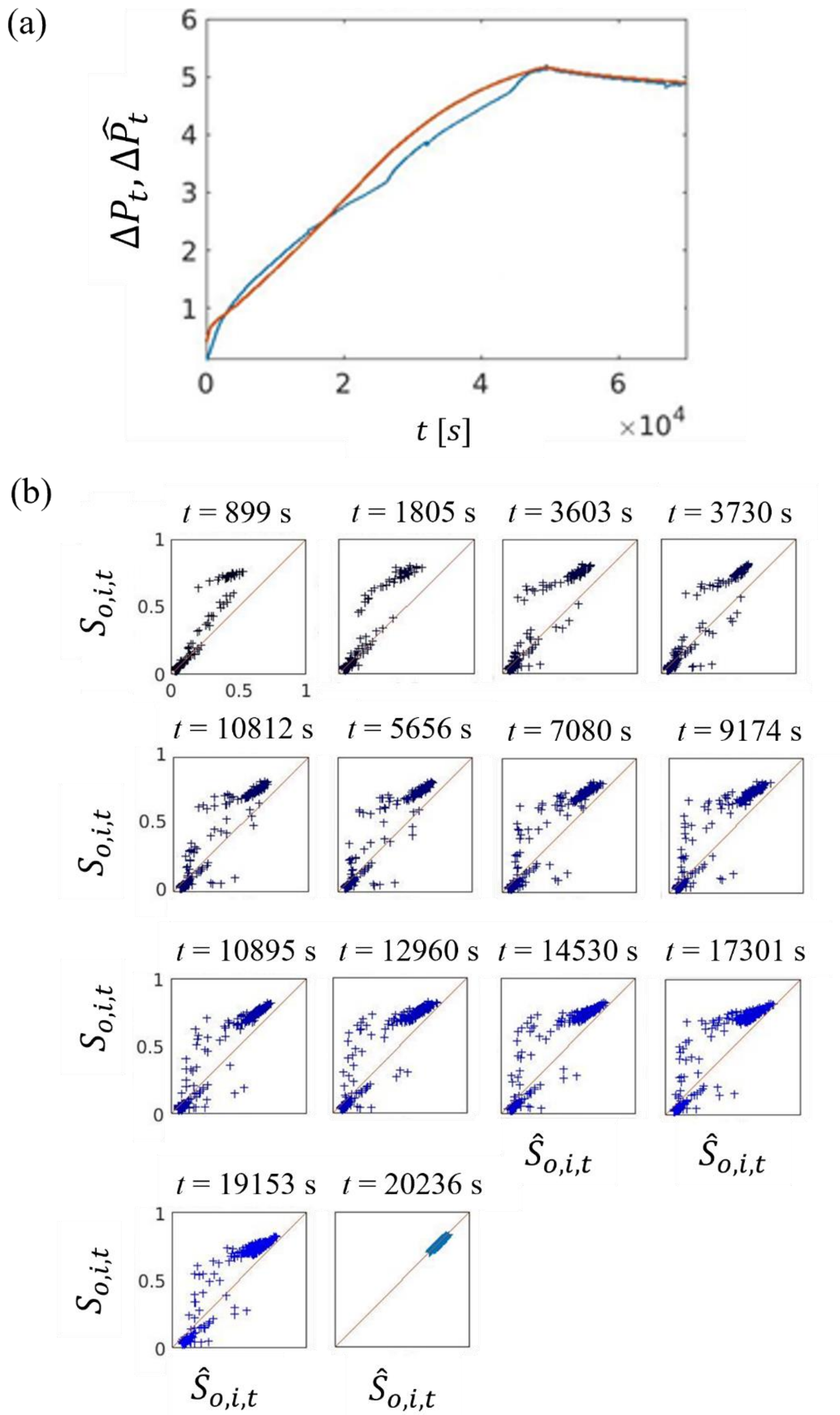

Fig. 6. Application of the proposed workflow for the brine-displacement scenario. Preliminary model calibration results: (*a*) experimental ($\Delta\widehat{P}_t$, blue curve) and numerical (ΔP_t, red curve) temporal pattern of core-scale pressure drop; (*b*) scatter plots of experimental oil saturations ($\hat{S}_{o,i,t}$) versus their numerical counterparts ($S_{o,i,t}$, symbols) at available observation times.

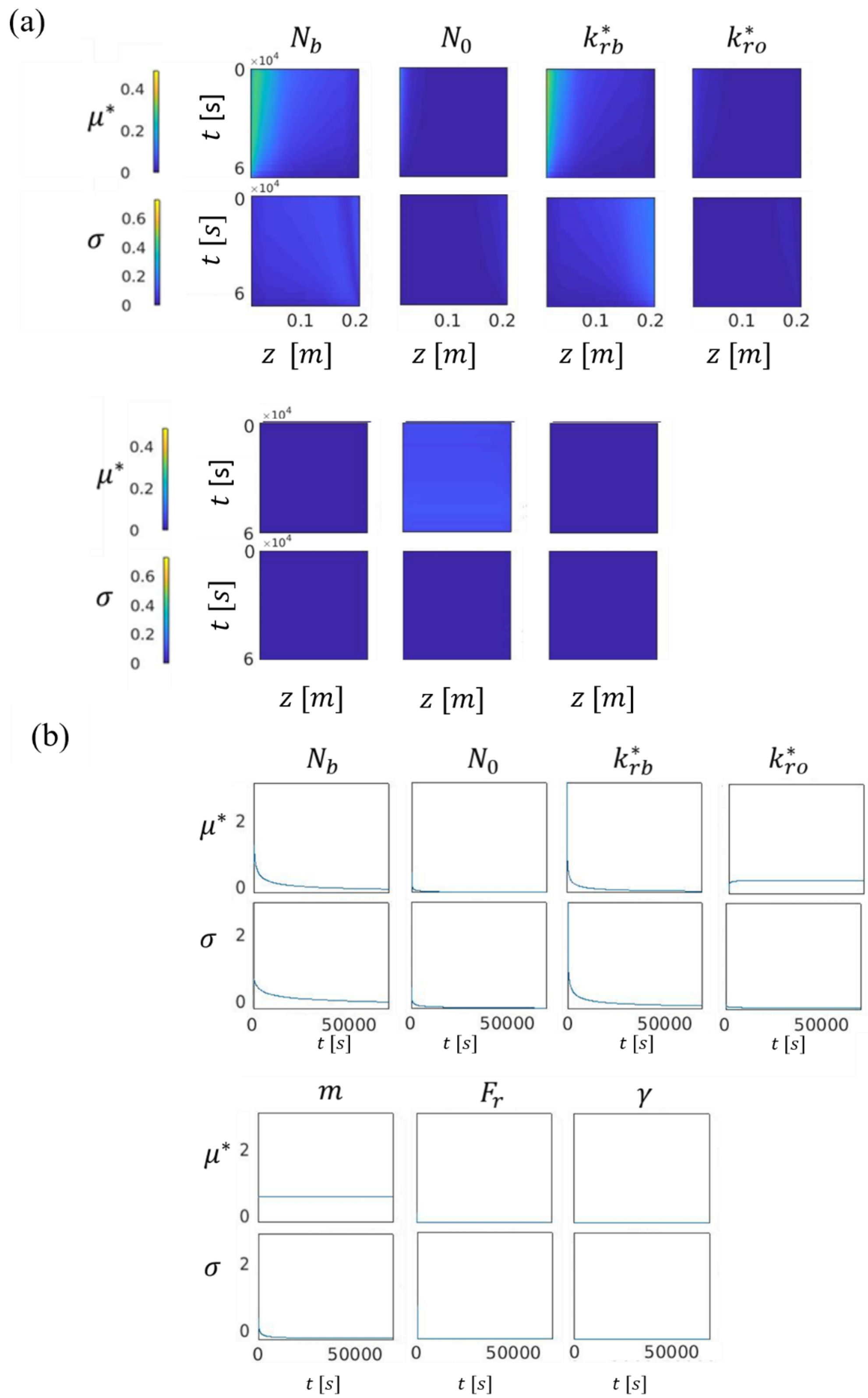

Fig. 7. Application of the proposed workflow for the brine-displacement scenario. Global Sensitivity Analysis results: Morris' sensitivity indices (i.e., $\mu^*_{\theta_j}$ (15) and σ_{θ_j} (16)) for (*a*) (section-averaged) oil saturation and (*b*) core-scale pressure drop.

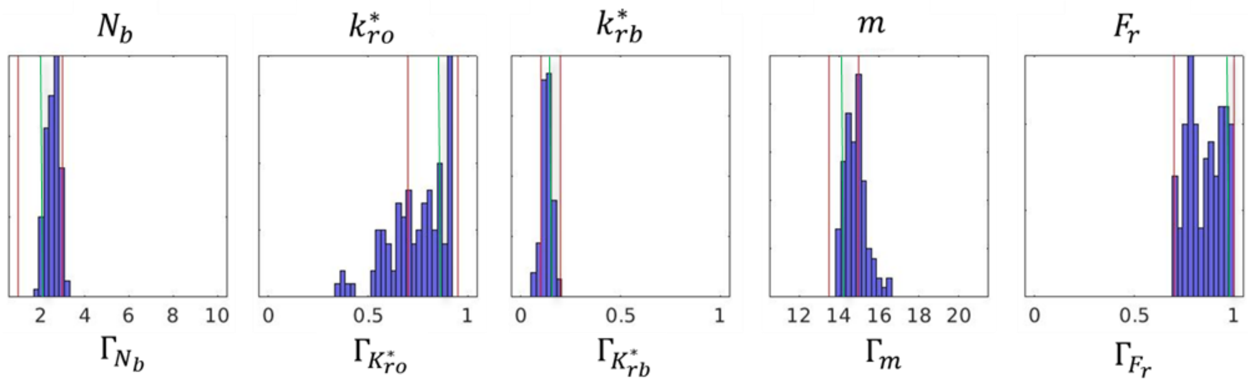

Fig. 8. Application of the proposed workflow for the brine-displacement scenario. Stochastic model calibration results: empirical frequency distributions for the set influential parameters (see Table 4). Red lines indicate the boundaries of the corresponding behavioral range; the green line correspond to the parameter values obtained through the preliminary model calibration stage.

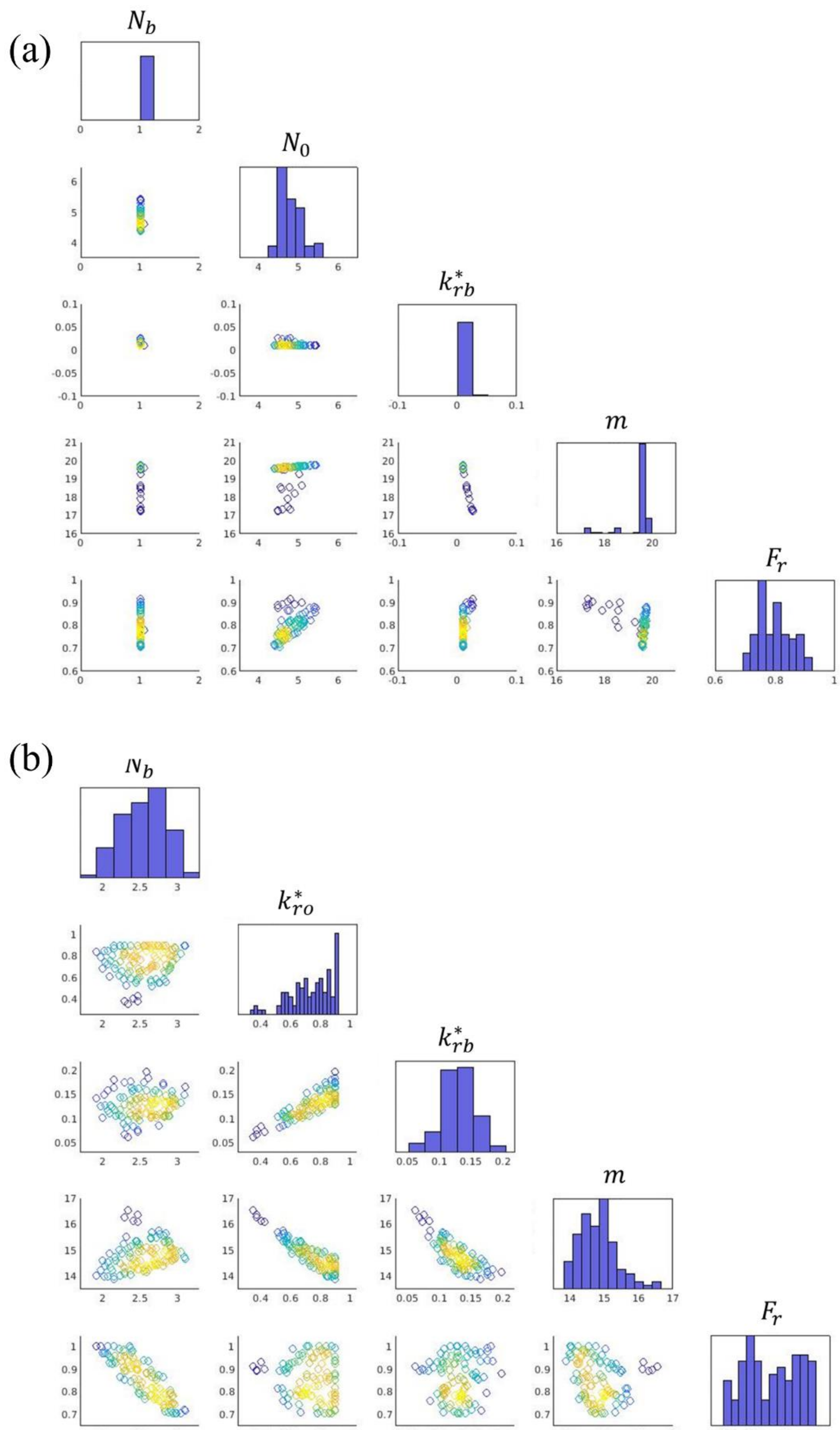

Figure A1. Scatter plot matrix for pairwise sets of parameter values stemming from stochastic model calibration considering the (*a*) oil and (*b*) brine displacement scenarios. Color gradation is indicative of the underlying bivariate probability function.

Tables

PROPERTY	SYMBOL	VALUE
LENGTH (cm)	l	20.1
DIAMETER (cm)	D	3.8
PORE VOLUME (ml)	PV	38.2
POROSITY (%)	$\langle\hat{\phi}\rangle$	16.7
ABSOLUTE PERMEABILITY (mD) AT BRINE SATURATION S_B = 1	K	31.0

Table 1. Key properties of the Berea sandstone core sample.

PROPERTY	SYMBOL	OIL-DISPLACEMENT EXP	BRINE-DISPLACEMENT EXP
OIL DENSITY (g/ml)	$\rho_{\boldsymbol{o}}$	0.76	0.86
OIL VISCOSITY (cp)	μ_o	1.41	93.2
BRINE DENSITY (g/ml)	ρ_b	1.13	1.13
BRINE VISCOSITY (cp)	μ_b	1.11	1.11

Table 2. Key properties of the fluids employed in the oil-displacement and brine-displacement experiments.

	PRELIMINARY MODEL CALIBRATION RESULTS	PARAMETER RANGE FOR SUPPORTS $\boldsymbol{\Gamma}$ AND $\boldsymbol{\Gamma'}$	PARAMETER RANGE FOR $\boldsymbol{\Gamma^B}$
$\boldsymbol{N_b}$	1.00	**[0-10]**	[0-2.5]
$\boldsymbol{N_o}$	4.73	**[0-10]**	[3.5-5.5]
$\boldsymbol{k^*_{rb}}$	0.09	**[0-1]**	[0-0.3]
$\boldsymbol{k^*_{ro}}$	0.01	[0-1]	[0-0.2]
$\boldsymbol{m}$	19.61	**[10-22]**	[15-22]
$\boldsymbol{F_r}$	0.78	**[0-1]**	[0.7-0.9]
$\boldsymbol{\gamma}$	146.76	[0-180]	[120-160]

Table 3. Results of the preliminary model calibration stage and ranges of model parameter values associated with the preliminary model calibration ($\boldsymbol{\Gamma}$), reduced ($\boldsymbol{\Gamma'}$, only bold ranges) and *behavioral* ($\boldsymbol{\Gamma^B}$) parameter spaces. Oil-displacement experiment.

	PRELIMINARY MODEL CALIBRATION RESULTS	PARAMETER RANGE FOR SUPPORTS $\boldsymbol{\Gamma}$ AND $\boldsymbol{\Gamma'}$	PARAMETER RANGE FOR $\boldsymbol{\Gamma^B}$
$\boldsymbol{N_b}$	2.02	**[0-10]**	[1-3]
$\boldsymbol{N_o}$	4.15	[0-10]	[3-5]
$\boldsymbol{k^*_{rb}}$	0.15	**[0-1]**	[0.1-0.2]
$\boldsymbol{k^*_{ro}}$	0.85	**[0-1]**	[0.7-0.95]
$\boldsymbol{m}$	14.01	**[10-22]**	[13.5-15]
$\boldsymbol{F_r}$	0.97	**[0-1]**	[0.8-1]
$\boldsymbol{\gamma}$	95.89	[0-180]	[80-100]

Table 4. Results of the preliminary model calibration stage and ranges of model parameter values associated with the preliminary model calibration ($\boldsymbol{\Gamma}$), reduced ($\boldsymbol{\Gamma'}$, only bold ranges) and *behavioral* ($\boldsymbol{\Gamma^B}$) parameter spaces. Brine-displacement experiment.

Declaration of interests

☐The authors declare that they have no known competing financial interests or personal relationships that could have appeared to influence the work reported in this paper.

☒The authors declare the following financial interests/personal relationships which may be considered as potential competing interests:

Alberto Guadagnini reports financial support was provided by Eni SpA. Aronne Dell’Oca, Martina Siena, Andrea Manzoni, Alberto Guadagnini has patent #4D-CoreINV software licensed to SIAE.

CRediT author statement:

A. Dell'Oca: Conceptualization, Methodology, Software, Validation, Formal analysis, Writing - Original Draft, Writing - Review & Editing; **A. Manzoni**: Conceptualization, Methodology, Software, Validation, Formal analysis, Writing - Original Draft, Writing - Review & Editing; **M. Siena**: Conceptualization, Methodology, Software, Writing - Original Draft, Writing - Review & Editing; **N. G. Bona:** Investigation, Data Curation, Writing - Review & Editing, Supervision; **L. Moghadasi:** Investigation, Data Curation, Writing - Review & Editing; **M. Miarelli:** Investigation, Data Curation, Writing - Review & Editing; **D. Renna:** Investigation, Data Curation, Writing - Review & Editing; **A. Guadagnini:** Conceptualization, Methodology, Validation, Formal analysis, Writing - Original Draft, Writing - Review & Editing, Supervision.